



MnO_x quantum dots decorated reduced graphene oxide/TiO₂ nanohybrids for enhanced activity by a UV pre-catalytic microwave method



Shiyi Cao^a, Chuansheng Chen^{a,*}, Juyan Zhang^b, Cui Zhang^b, Weiwei Yu^a, Bo Liang^a, Yuenhong Tsang^c

^a College of Physics and Electronic Science, State Engineering Laboratory of Highway Maintenance Technology, Changsha University of Science and Technology, Changsha 410114, China

^b Department of Microbiology and Immunology, Guangdong Pharmaceutical University, Guangzhou 510006, China

^c Department of Applied Physics, The Hong Kong Polytechnic University, Hong Kong 999077, China

ARTICLE INFO

Article history:

Received 8 February 2015

Received in revised form 15 April 2015

Accepted 18 April 2015

Available online 20 April 2015

Keywords:

MnO_x quantum dots

Reduced graphene oxide

UV preexcitation

Energy storing

Antibacterial activity

ABSTRACT

Graphene/TiO₂-based catalysts have attracted much attention as promising photocatalysts because of their low cost and excellent performance. In this report, we integrated the energy storage with high photocatalytic activity into a new model for wider applications in the field of energy utilization and environmental treatment. The MnO_x quantum dots were decorated on reduced graphene oxide/TiO₂ hybrids (GTM) by combining UV excitation with microwave method for the first time. Experimental results show that GTM nanohybrids have excellent photocatalytic activity for organic dyes under UV-vis light and good antibacterial activity. Besides, UV preexcitation can improve the adsorbability and photocatalytic durability of GTM nanohybrids for high-concentration dyes. These enhancements are attributed to the rapid separation of photogenerated carriers from reduced graphene oxide and surface defects induced by UV excitation, and the broad light absorption aroused by the narrow band gap and MnO_x quantum dots simultaneously.

© 2015 Elsevier B.V. All rights reserved.

1. Introduction

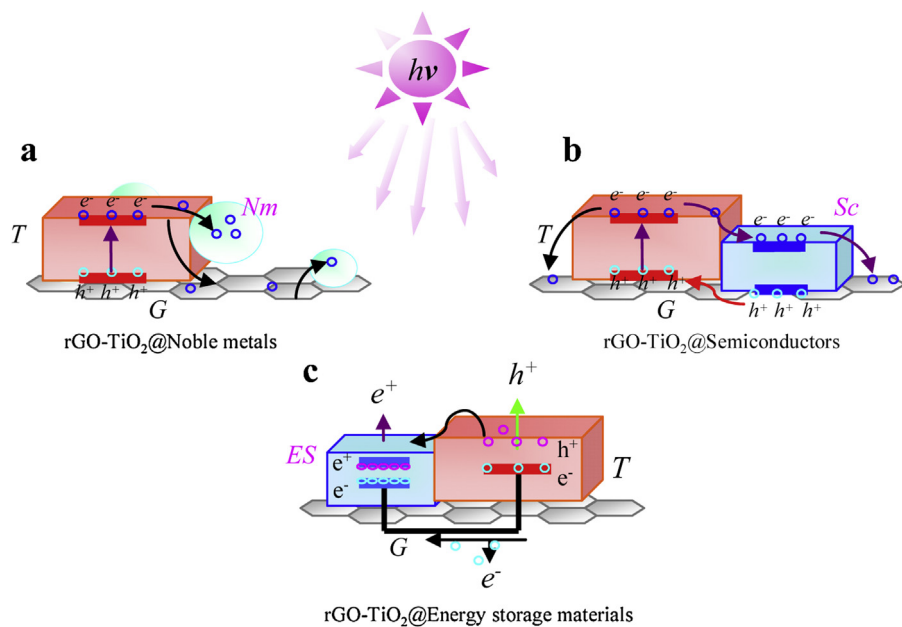
The light utilization and carrier separation are the most concerned issues of photocatalysts, especially for TiO₂ [1–4]. As a typical conductive supporter, graphene has been deemed as the most promising candidates to rapidly trap and transfer the photoinduced electrons of TiO₂ due to its high carrier mobility and larger electronic storage ability. For another, the large specific surface area about 2630 m² g⁻¹ in theory benefits to disperse TiO₂ nanoparticles [5–7].

To realize the performance improvement and comprehensive uses of graphene/TiO₂ composites in the hydrogen production or the treatment/disinfection of water and air, the graphene/TiO₂ based heterojunctions have been designed in various forms [8]. Recently, there are some reports about the graphene/TiO₂ based multi-composites, such as reduced graphene oxide/TiO₂-metal hybrids (rGO/TiO₂@Ag or Au or Pt) [9–12], Fe₂O₃/TiO₂/graphene

[13], SnO₂/TiO₂/graphene [14], CdS/TiO₂/graphene [15], Ag₃VO₄ [16] or Ag₃PO₄/TiO₂/graphene [17,18], and MoS₂/P25/graphene heterojunctions [19,20]. These heterojunction materials can be summarized and divided into two models: graphene/TiO₂@noble metal and graphene/TiO₂@semiconductor, as described in Scheme 1a and b, respectively. It is accepted that noble metal and graphene can trap the photogenerated electrons, and then transfer to other semiconductors, promoting the separation of electron–hole pair. Supposing to integrate the above models, wider light range absorption and higher efficiency would be maintained. However, compared to Fe₂O₃ and MnO_x [21], the expensive noble metal is still limited by its cost and toxicity. High efficiency for photocatalysts is impossible without continuous light irradiation in presence of the high carrier recombination. Therefore, importing energy-storing materials is helpful to store partial photogenerated electrons and enable the separation of charge carriers under light irradiation. Moreover, these stored electrons are released to work well under dark condition.

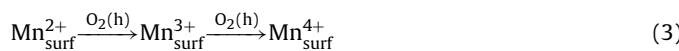
Manganese oxides (MnO_x) have received increasing focuses on lithium battery, supercapacitors and photocatalysts because of the high specific capacitance, large ion exchange capacity, cost

* Corresponding author. Tel.: +86 731 85258232; fax: +86 731 85258217.
E-mail address: jxccs1934@gmail.com (C. Chen).



Scheme 1. Model designs of graphene/TiO₂ based ternary photocatalysts, (a) rGO/TiO₂@noble metals, (b) rGO/TiO₂@semiconductors, (c) rGO/TiO₂@energy storage materials.

advantage and good redox activity [22,23]. It has been reported a strong O₂ activation to deal with organic contaminants and gas pollutions, such as alizarin yellow R [24], methylene blue [25], Hg⁰ adsorption [26] and NO_x removal [27]. In addition, the surface manganese ions can transform between Mn²⁺, Mn³⁺ and Mn⁴⁺ through reacting with photogenerated electrons and holes (or O₂) [28], as showed in Eqs. (1)–(4). However, rich MnO_x crystals suppress TiO₂ or ZnO photocatalysts in the treatment of water-soluble dyes [29], because their high electron-storing capacity may store excessive electrons and low conductivity is not favorable to the mobility and release of electrons [30–32]. Therefore, decorating graphene/TiO₂ with low MnO_x loading can capture and store the electrons or transfer the holes severally like an open-circuit nanoscale battery, and is available to improve the catalytic activity either in irradiation or in dark, as designed in Scheme 1c.



Considering these advantages of rapid synthesis, energy saving and environment friendly, novel energy-excitation methods including ultrasound, UV or visible light, laser and microwave, have attracted great attentions in the synthesis of nanomaterials. UV excitation has successfully deposited noble metal ions [33] and deoxidized graphene oxide [34]. In our previous report, the rGO/Bi₂Mo₃O₁₂@Bi₂O₃ heterojunctions showed the potentials of UV excitation method to prepare greenly graphene based photocatalysts at low temperature [35]. Simultaneously, microwave method has made much progress on yielding nanocrystals [36], such as TiO₂ [37], MnO₂ [38], graphene/TiO₂ [39] and graphene/MnO₂ [40]. In this work, the UV/H₂O₂ oxidation and microwave method (UV-MW) were combined to disperse MnO_x quantum dots on the reduced graphene oxide/TiO₂ hybrids (GTM) for the first time. UV preexcitation was found to activate the surface states and reduce graphene oxide, and consequently GTM hybrids showed great adsorbability, photocatalytic practicability and antibacterial effect. Therefore, the nanobattery model combining the energy storage of

MnO_x with the strong redox ability of TiO₂ on graphene can afford a new thought for design of photocatalysts for pollution treatment, solar cells and antibacterial agents.

2. Experimental

2.1. Preparation of rGO/TiO₂–MnO_x nanohybrids

Graphene oxide (GO) solution was made to a concentration of 2.0 g/L by the modified Hummer method. The typical procedure of rGO/TiO₂–MnO_x nanohybrids was described as follows. Briefly, 1.0 mL commercial acetic acid, 5.8 mmol tetra-*n*-butyl titanate, 2.0 mL polyacrylic acid (PAA, 20%), and 2.0 mL cetyltrimethyl ammonium bromide (CTAB, 1.0 mg/mL) were dispersed into 15.0 mL ethanol in order. Then 20 mL manganese acetate (0.05 mmol) dissolving with 1.0 mL concentrated HNO₃ was instilled, followed with 6.0 mL sonicated GO. After the pH was regulated to about 2–8 by 2.0 M NaOH, 20.0 mL mixture with 20 mmol H₂O₂ in distilled water was added dropwise, and subsequently the reactor was bathed in water at 60 °C for 30 min. UV light irradiation and microwave treatment (LWMC-20, 650 W) were conducted in flat-bottomed bowl with 100 mL solution and round-bottomed flask with 180 mL mixture for 30 min, respectively. Finally, after washed and filtered with distilled water for several times, the precipitates were dried and collected. In this work, pure TiO₂ and MnO_x were prepared as contrasts. The GO dosage from 0 to 12 mL, solution pH (value ~2.63–8.10) and Mn dosage (0.05–8.0 mmol) were served as the main factors.

2.2. Characterization

The thermogravimetric and differential thermal analysis (TG-DTA) was conducted by NETZSCH STA 409 analyzer in temperature range from 20 °C to 600 °C with a speed of 10 °C/min. The structure identification of samples was performed on the X-ray diffraction (XRD) measurement by Philips PW 1710 diffractometer with Cu K α 1 radiation, scanning from 10 to 75° with a speed of 5° per minute. The morphologies of sample were observed by a Hitachi S-4800 field emission scanning electron microscope (SEM). The elemental mapping was analyzed by a Tescan Mira3 field

emission scanning electron microscope in 20.0 kV. The microstructures and crystalline characters can be detected using a JEM-3010 transmission electron microscope (TEM) with an energy dispersive X-ray spectroscopy (EDS). X-ray photoelectron spectroscopy (XPS) was performed on a Thermo Scientific ESCALAB 250Xi. Raman spectra (Raman) were collected on a Renishaw inVia plus laser Raman spectrometer (UK) with an excitation laser wavelength of 532 nm (5 mW) at room temperature. The ultraviolet visible diffuse reflectance spectra (UV-vis DRS) of samples were tested on a Hitachi U-3010 spectrometer. The photoluminescence spectra (PL) of different samples were detected using a Hitachi F-4500 Fluorescence Spectrophotometer with excitation wavelength at 260 nm. The optical density (OD_{570nm}) of bacteria was recorded on a BioTek ELx800 microplate reader.

2.3. Photocatalytic test

Rhodamine B (RhB) and methyl orange (MO) were used as model dyes to evaluate the photocatalytic activity of rGO/TiO₂–MnO_x hybrids. The experiments were conducted in a self-made device under a 100 W high-pressure mercury lamp and 500 W Xe lamp for respective UV-light and visible-light photocatalysis. The typical procedures can refer to our previous reports [35]. Briefly, 100 mg catalysts were dispersed in 200 mL of 10⁻⁵ mol L⁻¹ (4.89 ppm) RhB or 200 mL of 20.0 mg L⁻¹ (20.0 ppm) MO solution, which was magnetically stirred without interruption to ensure the full suspension of particles. 5 mL solution was extracted, and subsequently centrifuged at 4000 rpm for 10 min. The absorbance of supernatant was collected by TU-2550 spectrophotometer at the maximum absorption wavelength of RhB (554 nm) and MO (464 nm).

The recycle tests were conducted after resetting dyes concentration by exchanging 3.0 mL of 489 ppm RhB or 20 mL of 200 ppm MO. The degradation ratio was calculated with (C/C_0) , where C_0 is the original concentration and C is the residual concentration at different time. According to the first-order kinetics equation, the reaction rate constant (k/min^{-1}) is consistent with the curve slope of $\ln(C_0/C) - t$.

2.4. Electrochemical measurement

All electrochemical measurements were performed in a 1.0 mol L⁻¹ Na₂SO₄ electrolyte at room temperature by a three-electrode setup. A platinum foil and a saturated calomel electrode (SCE) were used as the counter electrode and the reference electrode, respectively. The working electrodes were fabricated onto a nickel foam (1 cm × 1 cm) coating with samples, carbon black and poly(tetrafluoroethylene) in a mass ratio of 75:20:5. The cyclic voltammetry (CV) scanning from 0 to 1.0 V (vs. SCE) at different rates of 10, 20, 50, 100 and 200 mV s⁻¹, and electrochemical impedance spectroscopy (EIS) from 100 kHz to 0.01 Hz at open circuit potential, were measured by a CHI 660C electrochemical workstation.

2.5. Agar diffusion assay and antimicrobial coating

The antibacterial activity of samples was evaluated against *Staphylococcus aureus* (*S. aureus*), *Escherichia coli* (*E. coli*) and natural bacteria by the agar diffusion method and coating method. All procedures were performed in a sterilized condition. The agar plates were first inoculated uniformly with 100 μL *S. aureus* or *E. coli* (~10⁶ cfu/mL). The high-pressure photocatalysts were dissolved into 10 mL sterile saline solution, sonicated for 30 min, and diluted to 250, 125, 62.5, 31.25 and 15.62 μg/mL. The sterile papers (6 mm) dipping with above suspension were irradiated under UV light for 30 min, and subsequently implanted on the agar plates. For another, 100 μL UV-irradiated catalysts suspension were uniformly

coated on the agar plates and inoculated with the indoor bacteria for 30 min. Finally, these agar plates and coating plates were cultivated in dark at 37 °C for 18 h. For comparison, normal saline paper and penicillin paper (10 μg) were conducted. The size of inhibition zone, colonies number and the minimum inhibition concentration (MIC) were used as the evaluation of antibacterial effect.

2.6. Growth curve study

The growth dynamics of *S. aureus* and *E. coli* were studied in presence and absence of GTM hybrids. 100 μL of fresh bacterial culture (10⁶ cfu/mL) was inoculated in the 96-well tissue culture plates containing 100 μL broth medium. Afterwards, the sonicated GTM suspensions (0–250 μg/mL) were added and irradiated under UV light for 20 min. The culture plates were incubated at 37 °C for 0–4 h, followed with importing 20 μL thiazolyl blue (MTT, 5 mg/mL). After setting for another 4 h until the complete crystallization, 100 μL dimethyl sulfoxide (DMSO) was used to dissolve these crystals. The optical density (OD_{570nm}) of bacterial solution was used to evaluate the numbers of active bacteria, and MIC was used to evaluate the antibacterial activity.

3. Results and discussion

3.1. Characterization of catalysts

The rGO/TiO₂–MnO_x hybrids were synthesized by the combination of UV/H₂O₂ oxidation and microwave method (UV-MW), as expressed in Fig. 1a. The color was changed from transparent to increasing black after instilling GO, gradually into gray with titanium hydroxide colloid formed by modulating pH uniformly up to 2.83 (Fig. 1b). Yellow suspension was shaped at pH ~2.83 when H₂O₂ was imported, which was recognized as peroxy-titanium complex (PTC: Ti(O₂)₂ or TiO(OH)₂) [42,43]. The yellow was faded under UV irradiation, and then changed into gray or black after microwave radiation. Microwave irradiation can couple directly energy with the molecules heating up uniformly to 200–250 °C in one minute (Fig. 1c) [41]. Assuming 40–80% of microwave working (W) converting into solution (Q), the heating temperature can reach 210.7–421.4 °C according to Eqs. (5)–(6). In this case, the yellow PTC should be decomposed to TiO₂, and at same time graphene oxide can be reduced in situ [44,45].

$$Q = Cm(T - T_0); W = P \times t; \quad (5)$$

$$Q = W \times \eta; \\ T = T_0 + \frac{P \times t \times \eta}{C \times m} \quad (5)$$

$$(T_0 = 25^\circ\text{C}, t = 30 \times 30\% \text{ min}, C_{\text{solution}} > C_{\text{H}_2\text{O}} = 4200 \text{ J kg}^{-1} \text{ C}^{-1},$$

$$m_{\text{solution}} > m_{\text{H}_2\text{O}} = 180 \text{ g}, P = 650 \text{ W}, \eta = 40 - 80\%) \quad (6)$$

To simulate the phase transformation during microwave irradiation, DTA-TG tests were conducted in temperature range of 0–600 °C over TiO₂, MnO_x and rGO/TiO₂–MnO_x. As Fig. 2a revealed, the mass loss before 150 °C with the endothermic peak at ~100 °C is responsible for the removal of adsorbed water. The oxidation of PTC and organics occurred at 207–283 °C. Mass loss details in DTG curves (Fig. 2b) show the transition of amorphous manganese–titanium oxides at 350–400 °C. The comparison of peak intensity in DTG indicates that GTM hybrids are composed of TiO₂ crystals, little MnO_x and PTC, which is confirmed by XRD patterns as shown in Fig. 2c. Similar diffraction peaks matching anatase TiO₂ (JCPDS no. 21-1272) can be seen in pure TiO₂, rGO/TiO₂,

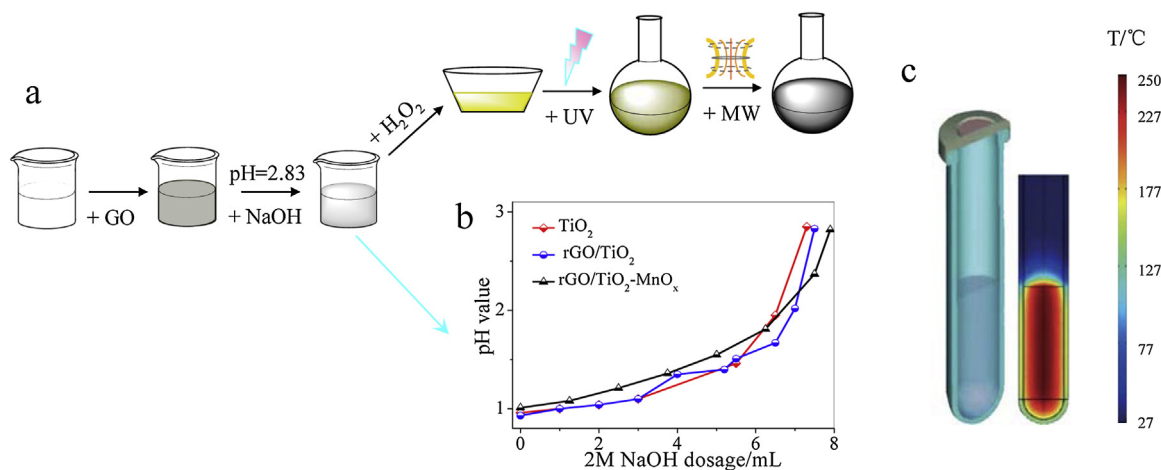


Fig. 1. (a) Schematic diagram for UV-WM procedure of GTM, (b) the curve of pH change vs. NaOH dosage in synthesis, and (c) temperature gradients and profiles after 60 s of microwave irradiation [41].

and rGO/TiO₂-MnO_x. Pure MnO_x is consistent with hausmannite Mn₃O₄ (JCPDS no. 24-0734). No sign of manganese oxide and rGO is detected because of the low manganese loading and GO content.

Raman spectra were used to further confirm their structure and seen in Fig. 2d. The observed characteristic peaks at 151, 403, 517, and 646 cm⁻¹ are consistent with 142 (E_g), 394 (B_{1g}), 515 (A_{1g}+B_{1g}) and 639 (E_g) of anatase TiO₂ [12,46]. After importing graphene, two characteristic peaks for D and G mode of graphene oxide can be observed at 1335 and 1600 cm⁻¹, respectively [47], which also can be seen in rGO/TiO₂ and GTM. In particular, there exists little red shift in characteristic peaks of TiO₂ and blue shift in D and G band of graphene oxide, suggesting the presence of Ti—O—C band. The intensity ratio of D and G band (I_D/I_G) in GO, rGO/TiO₂ and GTM is 1.014, 0.896 and 0.884, respectively, indicating the obvious increase of sp² domain and the reduction of GO [44]. In addition, Raman

spectrum of pure MnO_x shows four peaks at 297, 354, 576 and 643 cm⁻¹ assigning to the oxygen vibrations of MnO_x (MnO₂ [48,49] or Mn₃O₄ [50]).

In order to detect the state of different elements in GTM hybrids, the core level XPS spectra of C, O, Ti, and Mn were carried out. Fig. 3a demonstrates that the three fitting peaks with binding energies at 284.8, 286.66 and 288.56 eV, are referred to the non-oxygenated ring C, C—O bonds or C—OH bonds, and COOH, respectively [51]. The peaks at 531.6 and 532.99 eV from the core level O 1s spectrum (Fig. 3b) are corresponding to the —OH and O vacancies [52,53]. As shown in Ti 2p XPS spectra (Fig. 3c), two main peaks centered at 458.39 and 464.15 eV are responsible for Ti 2p_{3/2} and Ti 2p_{1/2}. Two fitting peaks at 460.41 and 466.25 eV may be indexed to the interface bonding of Ti—O—C and Ti—OH. Meanwhile, four peaks at 636–654 eV in Fig. 3d reveal that

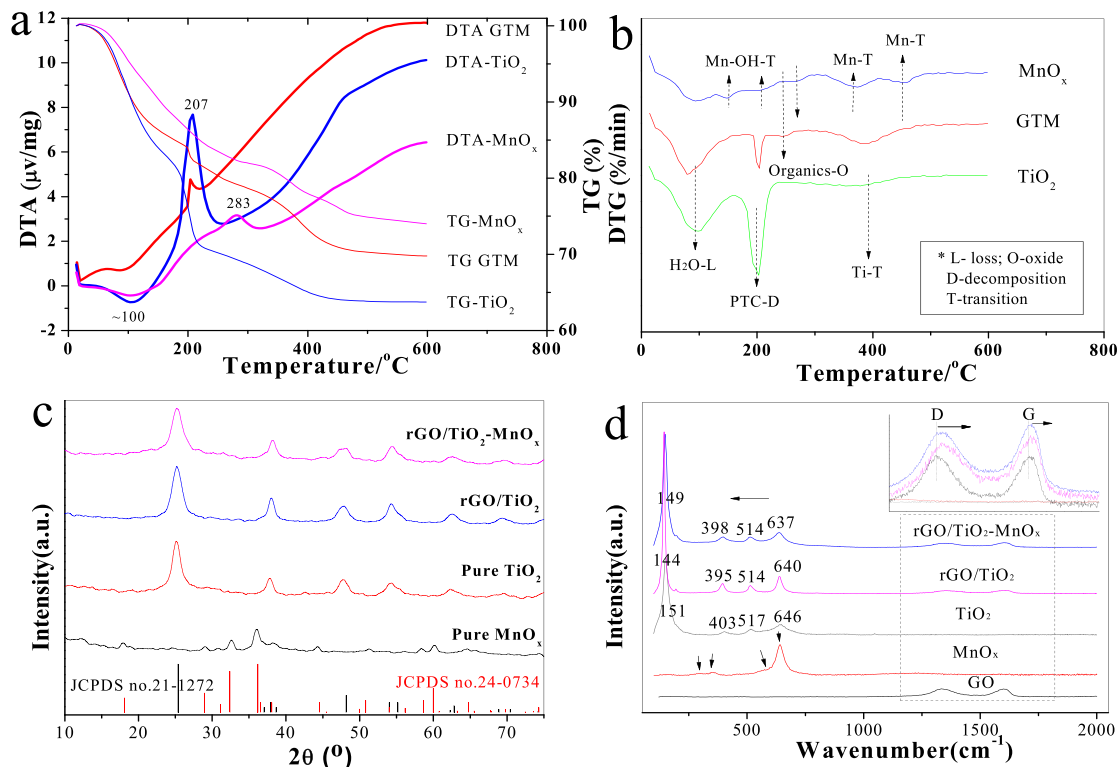


Fig. 2. (a) TG-DTA curves and (b) DTG curves of TiO₂, MnO_x, and rGO/TiO₂-MnO_x, (c) XRD patterns and (d) Raman spectrum of pure TiO₂, rGO/TiO₂, and rGO/TiO₂-MnO_x.

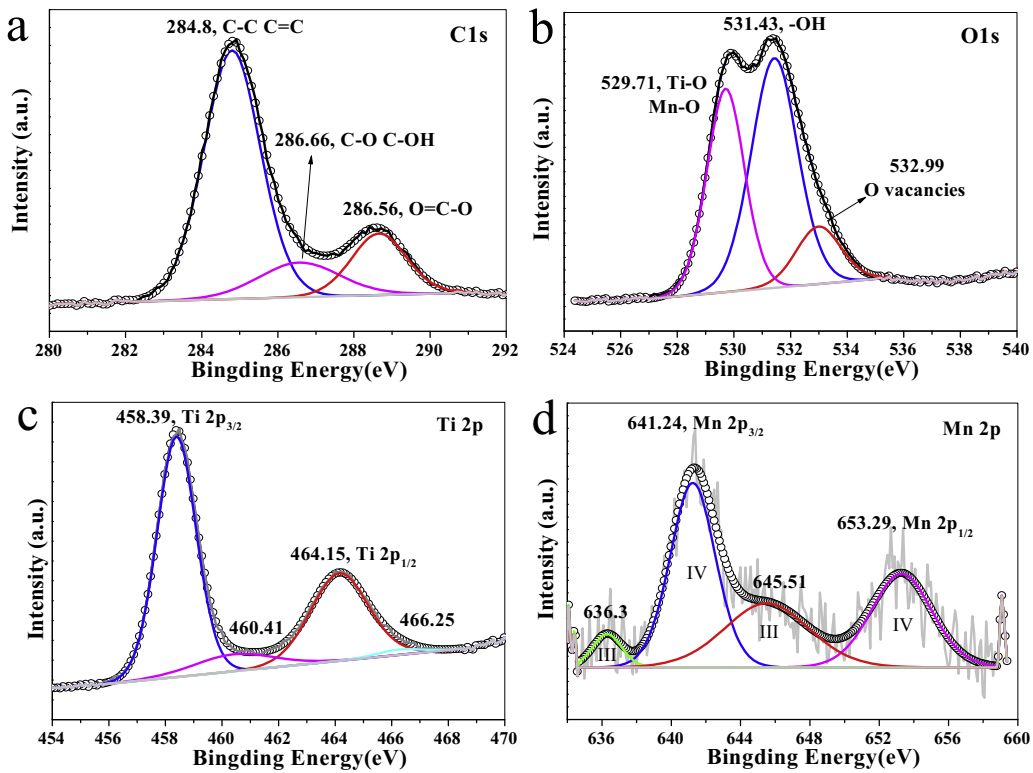


Fig. 3. Core level XPS spectra of (a) C 1s, (b) O 1s, (c) Ti 2p and (d) Mn 2p of GTM nanohybrids.

GTM contains 31.3% Mn(III) and 68.7% Mn(IV), equivalent to 53.1% MnO_2 and 15.6% Mn_3O_4 from the fitting area, similar with the Ref. [54–56].

SEM images of Ti-related samples (Fig. 4a–d) depict big flat surface due to the formation of peroxy-titanium complex, compared to GTM without H_2O_2 treated (Fig. 4e). Many multi-layer stacks can be observed in MnO_x and remained in the hierarchical structure in Mn-related samples (Fig. 4c–f). Further TEM characterization in Fig. 5a describes that many nanoparticles are covered uniformly on graphene. To figure out the causes of flat surface, two sites were selected in high-resolution TEM (HRTEM). Fig. 5b displays the microstructure of middle section with some interplanar space about 0.235 nm and 0.34 nm identified to (2 1 1) plane of MnO_2 quantum dots (QDs) and TiO_2 (1 0 1) plane [57], respectively. However, more (1 0 1) crystal face of TiO_2 with d -spacing of 0.351 or 0.362 nm are exposed on the edge of GTM hybrids in Fig. 5c. Meanwhile, little MnO_2 and Mn_3O_4 crystals can be recognized (marked in yellow). Two SAED images of different position confirm the presence of anatase TiO_2 , but their difference reflects more complete diffraction information of TiO_2 on surface. The possible reason is that more PTC formed at surface and transformed into TiO_2 after absorbing with microwave energy. In addition, EDS result (Fig. 5d) proves the GTM with a low load of MnO_x , where the average Ti/Mn ratios is 10.6:1 with 1.11% Mn content, leading to no clear sign in DTA-TG, XRD and Raman results of GTM hybrids.

To illustrate the spatial distribution of different elements in GTM hybrids, the SEM and elemental mapping in a big bulk region have been performed. As observed in Fig. 6, the selected bulk part comprises the elements of C, O, Ti and Mn with the average Ti/Mn ratio of 9.31 and 0.85% Mn, in agreement with the previous results. In the elemental mapping of GTM, the C, O, Ti and Mn are well dispersed. In addition, more TiO_2 and little MnO_x can be detected on surface of GTM nanohybrids.

3.2. Effect of technical parameter on photocatalytic activity

In principle, either the holes or free radicals ($\cdot\text{OH}$, $\text{H}_2\text{O}^\bullet$, H_2O_2) serve as the main oxidizing agents in photocatalysis. The strong adsorbability coupling with holes or the mild one combining with free radicals accesses a high activity, while excessive adsorption results in thick dye covering on the surface and a lower light transmissivity. Therefore, the compatibility of adsorbability and oxidants should be considered during the photodegradation. It is generally found that TiO_2 -related photocatalysis mainly depends on the free radicals [58,59]. In this study, GTM composites have been proven certain compatibility of adsorption and oxidization, as given in Fig. 7a. Slow adsorption process happened within 50 min in dark and consequently 35% of RhB was adsorbed, while 29.2% of RhB was adsorbed after 20 min. Subsequently both of residual RhB of two conditions were degraded after UV irradiation for 30 min. The similar result suggests that 20 min should be a reasonable adsorption time for better comparison of different samples. In particular, the difference of curve slopes during the adsorption and photocatalysis indicates that the later plays a more important role in organics removal.

The Mn loading, H_2O_2 , pH and graphene contents are supposed to be the main significant factors. Fig. 7b reveals that TiO_2 accelerates the photodegradation of RhB, but MnO_x impedes this process compared to the pure UV light, similar as the report in Ref. [29]. However, in the presence of graphene, the photocatalytic activity was remarkably enhanced, and further incorporating MnO_x with rGO/ TiO_2 obtained the optimal activity. In addition, different Mn mole% usage at synthetic pH 4 makes restraint effect on rGO/ TiO_2 according to the k histogram in Fig. 7b. These results confirm our previous speculation that low MnO_x modification is favorable to enhance the activity. From another aspect, Mn loading and Ti hydrolysis are positively related to the pH condition. To further study the effect of pH or Mn loading

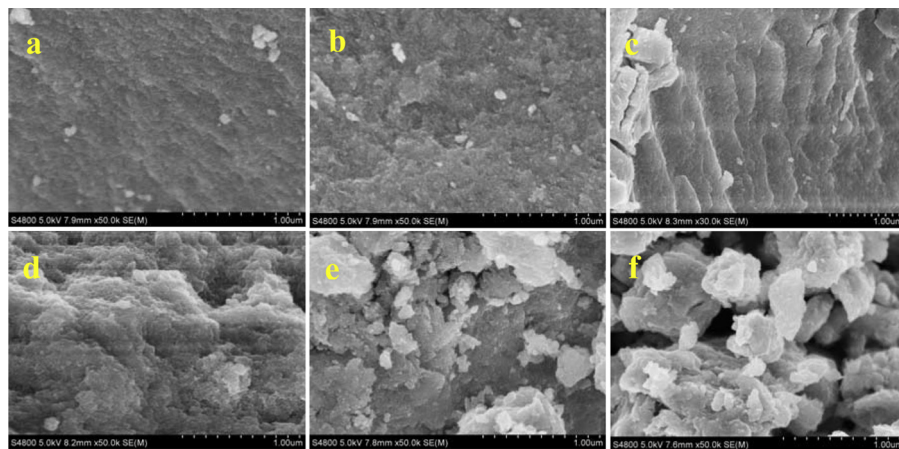


Fig. 4. SEM images of (a) TiO_2 , (b) rGO/ TiO_2 , (c) $\text{TiO}_2/\text{MnO}_x$, (d) rGO/ $\text{TiO}_2\text{--MnO}_x$, (e) rGO/ $\text{TiO}_2\text{--MnO}_x$ without H_2O_2 treated, and (f) MnO_x .

on GTM hybrids, the reaction rate (k) of GTM synthesized with different pH in presence and absence of H_2O_2 was compared in Fig. 7c. The activity of GTM treated at different pH follows with the order: $2.83 \approx 3.02 > 2.63 > 3.3 \approx 2.56 > 3.9 > 6.21 > 8.01$. Simultaneously, the marked decline trend of k is found at pH ranging from 2.83 to 3.63 in results of GTM prepared without H_2O_2 . As a result, it can be summarized that low pH or Mn ions level is more attractive to enhance the photocatalytic activity of rGO/ TiO_2 . Especially, owing to the possibility of surface hydroxyls and O vacancies induced by UV/ H_2O_2 oxidation, higher catalytic rate can be seen in result of GTM hybrids with H_2O_2 -assisted synthesis. These active species are deemed to prolong the conduction life of photoinduced electron and hinder the electron–hole pairs recombination [60].

As an excellent supporter, suitable graphene can significantly improve the activity of semiconductors. Fig. 7d reveals the effects of graphene oxide dosage on the photocatalytic activity of GTM hybrids under different manganese ion level. The experiments prove that little rGO can enhance the photocatalytic activity of

L-GTM nanohybrids, and the optimal use of GO is 6–8 mL when $0.1 \text{ mmol/L Mn}^{2+}$ is employed. Lower degradation rate can be observed if GO is excessive to 8–12 mL. This is because overloaded graphene acts as the conductive bridge of charge carriers, increasing the recombination possibility of electron and hole pairs [35]. Similar phenomenon was found in H-GTM assisted with $4.0 \text{ mmol/L Mn}^{2+}$, but notably the optimal H-GTM shows the better activity, increased by a factor of 1.6 than that of L-GTM. This obvious ups and downs of activity is possible in that GO or Ti precursor enable to adsorb many Mn^{2+} with more MnO_x loading increased when high-concentration Mn^{2+} is used.

For practical purpose, loading nanoparticles on graphene to build bulk materials is effective to improve the recovery and recycle of nanocomposites. Fig. 8a displays five recycles of RhB over GTM under UV irradiation. The total RhB can be completely decomposed within 30 min coupling with the degradation ratio of 100%, 100%, 100%, 100% and 98.2%, respectively. In addition, GTM can remove MO dyes rapidly in contrast with UV irradiation, and there exhibits good durability in the repeated irradiation for 180 min, as

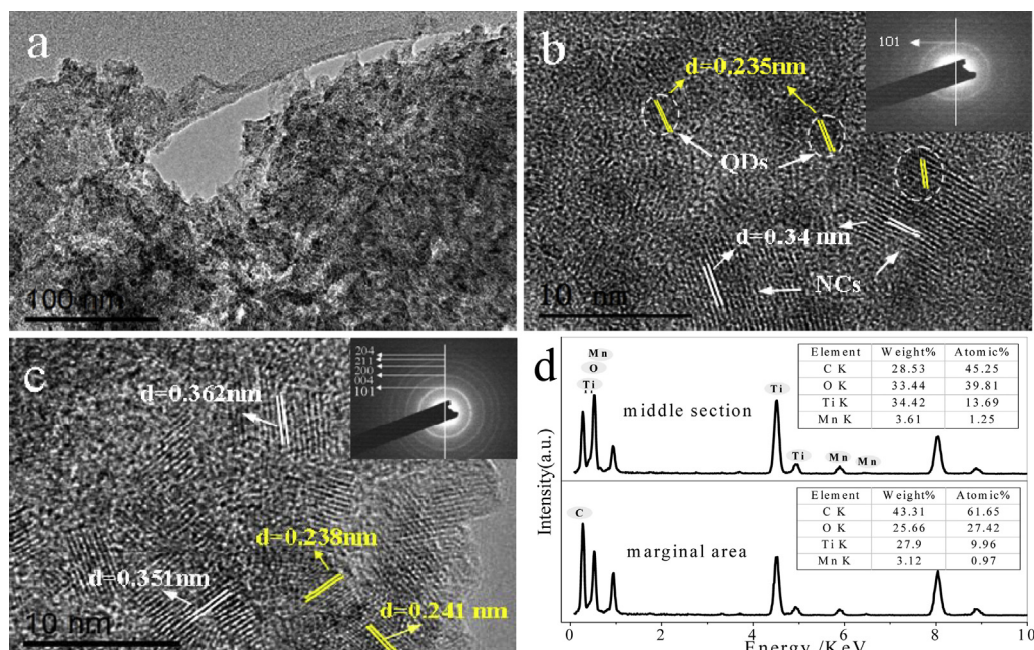


Fig. 5. (a) TEM image, (b) HRTEM image and SAED of GTM in middle section, (c) HRTEM image and SAED of GTM at marginal area, and (d) EDS of GTM. (For interpretation of the references to color in this figure text, the reader is referred to the web version of this article.)

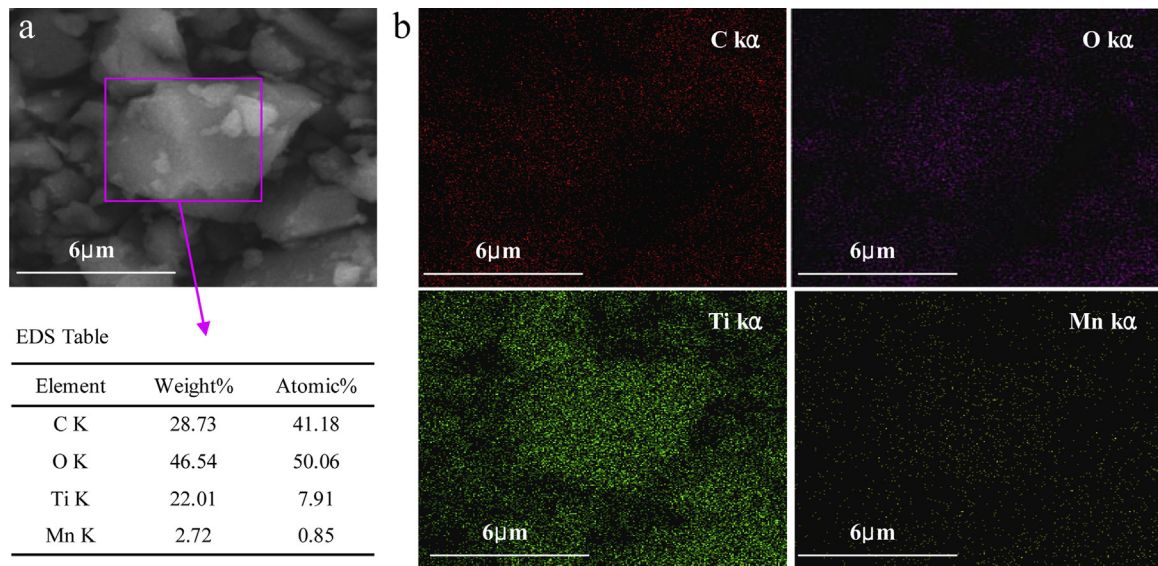


Fig. 6. (a) SEM image and EDS table, (b) element mapping of C, O, Ti and Mn.

recorded in Fig. 8b. These results indicate that GTM hybrids have a great stability under UV irradiation. Furthermore, we measured the visible-light activity and recyclability of GTM by degrading RhB under Xe lamp. Fig. 8c announces that 7 h irradiation of pure

visible light can discolor 11.8% of RhB, while GTM can significantly promote to degrade 94.3% of RhB. Then little declines of degradation ratio to 80.8% and 68.3% are recorded in the following recycles owing to the residual RhB and the surface O vacancies or hydroxyls

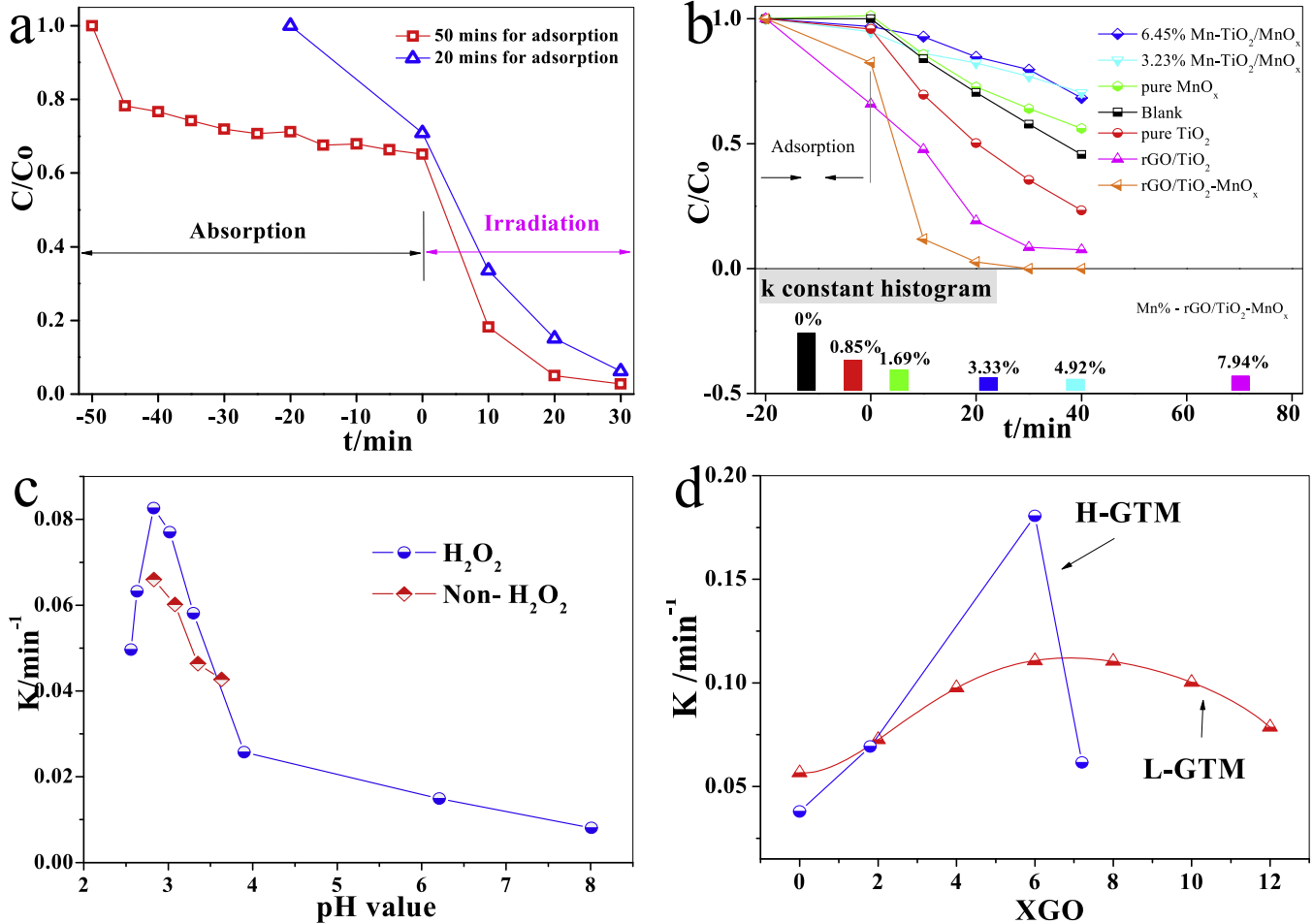


Fig. 7. (a) The adsorption and photodegradation of RhB over GTM, (b) the photocatalytic results of different samples; reaction rate k of GTM: (c) effect of pH and (d) effect of GO usage on L-GTM and H-GTM with respective Mn²⁺ concentration of 0.1 and 4.0 mmol/L.

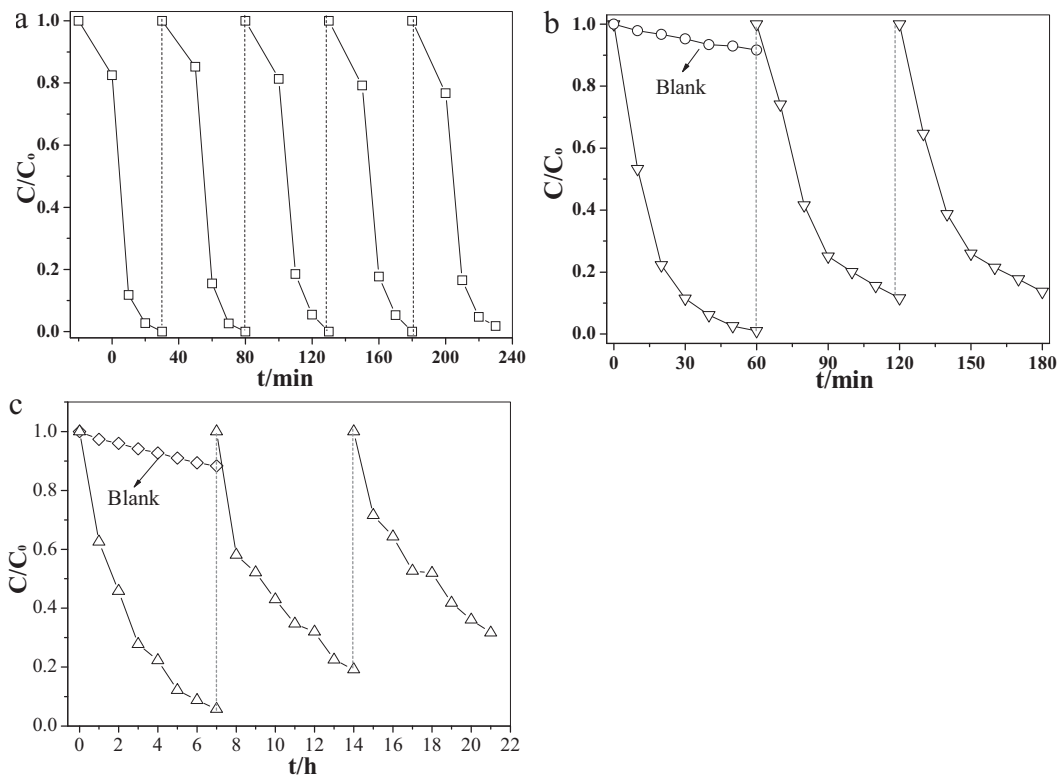


Fig. 8. (a) The recycle degradation of RhB under UV light, (b) the recycle degradation of MO under UV light, and (c) the recycle degradation of RhB under visible light.

without enough supplements under visible light, compared to UV light.

To be summary, the fine control of graphene oxide, Mn-ions level, pH and other condition can earn the high reproducibility and great efficiency of organics' degradation, suggesting that graphene-based $\text{TiO}_2/\text{MnO}_x$ hybrids have potential applications in environment treatment.

3.3. Electrochemical energy-storing measurements

Fig. 9a illustrates the specific capacitance of MnO_x , $\text{TiO}_2/\text{MnO}_x$, and $\text{rGO}/\text{TiO}_2-\text{MnO}_x$ at different scan rate. MnO_x shows the high specific capacitance but a low stability, similar to the Ref. [64,65]. TiO_2 can increase the stability of system because of its high chemical stability, and graphene induces a further improvement on $\text{TiO}_2/\text{MnO}_x$ using its excellent electronic storage. Importantly, there can be seen low specific capacitance and no clear change of specific capacitance at various scanning speeds in $\text{TiO}_2/\text{MnO}_x$ and GTM electrodes, which can be resulted from the low content of Mn (average 1.11% in GTM) and Ti-related bulk structure. The electron transfer of samples is estimated by EIS (Fig. 9b), in which the nyquist plots of all three electrodes contain a semicircle at high–medium frequency and an inclined line at low frequency referring to charge transfer and diffusion, respectively. The transfer resistances (R_{ct}) of MnO_x , $\text{TiO}_2/\text{MnO}_x$ and $\text{rGO}/\text{TiO}_2-\text{MnO}_x$ electrodes are 78.49, 5.424 and 2.488 ohm. It means that TiO_2 can increase the conductivity of $\text{TiO}_2/\text{MnO}_x$ and graphene further facilitate the electrons transfer to a great extent [57]. Thus, GTM hybrids show the highest photocatalytic activity. To further study the stability of GTM, CV and EIS recycling were tested. Little change of CV shape and a decrease of redox potential are recorded in Fig. 9c and slightly increased impedance of R_{tc} and Wurb resistance (δ) during the EIS recycling are observed in Fig. 9d. These changes should be due to the ionization and migration of Mn from surface MnO_x to solution. Hence, in

the catalytic process, this migration led to the activity decreases of photocatalysts with the recycle times.

3.4. UV-preexcitation for enhanced photochemical energy storage

In this work, UV irradiation has been successfully applied as an assisted method to synthesize rGO-based hybrids. To find out this functional mechanism, the photocatalytic properties of GTM and UV-preexcited GTM hybrids were studied and presented in Fig. 10. The adsorption ratios of RhB (4.98 ppm) is increased obviously from 9.6% to 69.3% after UV preexcitation for 10 min with a clear color fading revealed in the inset photograph, and subsequently a-GTM can remove RhB in shorter time under UV light irradiation. In addition, the adsorbability and photoactivity of GTM and a-GTM samples were compared by serial photocatalytic tests increasing concentration of RhB from 4.89 to 12.00 ppm. Clearly, compared to GTM, the a-GTM displays greater adsorbability and higher efficiency of treating different-concentration RhB dyes, indicating that a-GTM samples have great durability and stability under UV light. As a result, GTM can absorb and store the photochemical energy of UV light, following with increased adsorbability and photoactivity. The UV irradiation can serve as one of activation methods for enhancing photocatalysts.

3.5. Photochemical storing energy for antimicrobial activity in dark

Biological environmental factors play a direct or indirect role on the adsorption and photodegradation of heterogeneous catalysis [61,62]. There are increasing needs for antibacteria under light irradiation and especially in dark condition. In this report, more attentions were focused on the antimicrobial effect without light to verify the energy-storing ability. Most test data on the samples without UV-activation showed no significant differences of inhibition effect with the normal saline (NS), inferior to

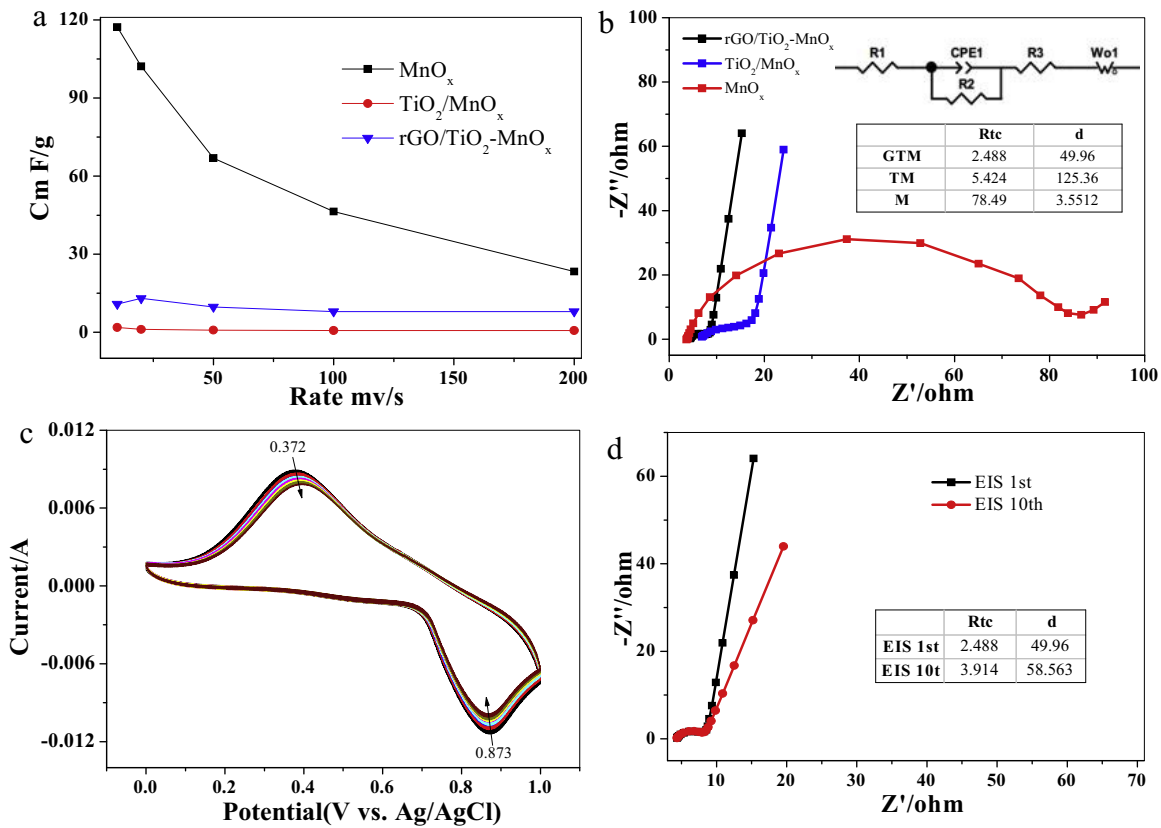


Fig. 9. (a) Specific capacitance of MnO_x , $\text{TiO}_2/\text{MnO}_x$, and GTM at different scan rate; (b) EIS plots, (c) CV recycle curves of GTM at scan rate of 10 mV s^{-1} and (d) recycling EIS plots of GTM.

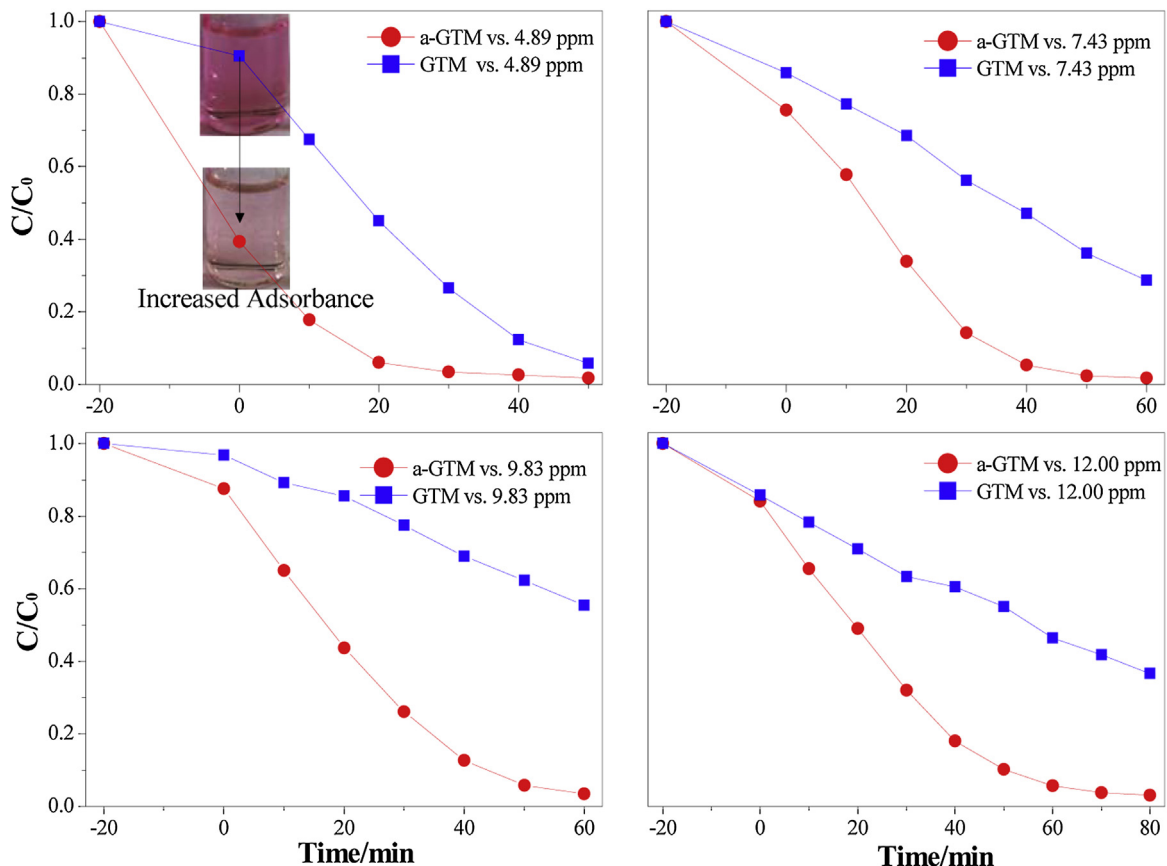


Fig. 10. Comparison of adsorption and photodegradation of different concentration RhB from 4.89 to 12.00 ppm over GTM and pre-excited GTM (a-GTM).

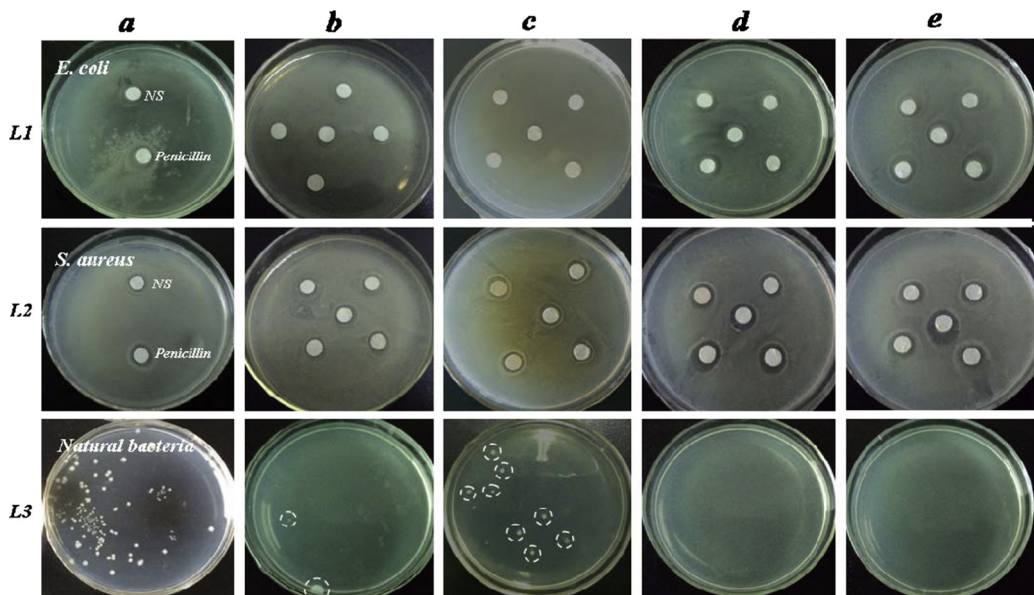


Fig. 11. The photocatalytic activity for antimicrobial in dark over (a) saline control and penicillin control group, pre-excitated samples: (b) TiO_2 , (c) MnO_x , (d) rGO/TiO_2 , and (e) $\text{rGO}/\text{TiO}_2-\text{MnO}_x$.

Table 1

Optimum IC, MIC ($\mu\text{g}/\text{mL}$) and inhibition zone (mm) of different samples against *S. aureus* and *E. coli*.

| Sample types | Optimum IC and MIC $\mu\text{g}/\text{mL}$ | | Inhibition zone (mm) | |
|--|--|------------------------|--------------------------|------------------------|
| | Against <i>S. aureus</i> | Against <i>E. coli</i> | Against <i>S. aureus</i> | Against <i>E. coli</i> |
| Control group | — | — | 9.026 | 10.714 |
| TiO_2 | 250 (125) | >250 | 9.185 (9.126) | >8.988 |
| rGO/TiO_2 | 62.5 (15.62) | 250 (250) | 14.330 (10.714) | 10.893 (10.893) |
| $\text{rGO}/\text{TiO}_2-\text{MnO}_x$ | 250 (15.62) | 125 (31.25) | 14.884 (10.554) | 13.008 (10.915) |

the penicillin. However, UV irradiation induced prominent inhibition effect, as the results were demonstrated in Fig. 11. In the agar diffusion test of *E. coli* (L1) and *S. aureus* (L2), as-prepared TiO_2 (Fig. 11b) shows the inhibition rings size against *E. coli* and *S. aureus* between normal saline group (NS) and penicillin (Fig. 11a). MnO_x seems to display bigger inhibition rings, but carefully some bacteria were found to grow around the discs (Fig. 11c). The amorphous MnO_x could be suitable for bacterial growth owing to the compatibility of surface oxygen defects. Graphene improves significantly the antimicrobial activity of TiO_2 and arouses big inhibition zones equals to that of penicillin (Fig. 11d). The bigger zones can be observed in different-concentration $\text{rGO}/\text{TiO}_2-\text{MnO}_x$ discs (Fig. 11e), suggesting the further improvement of MnO_x QDs. In terms of the above results, the optimum inhibition concentration and minimum inhibition concentration (MIC) were summarized in Table 1. The MIC shows 125 $\mu\text{g}/\text{mL}$ of TiO_2 , 15.62 $\mu\text{g}/\text{mL}$ of rGO/TiO_2 and 31.25 $\mu\text{g}/\text{mL}$ $\text{rGO}/\text{TiO}_2-\text{MnO}_x$ are sufficient for *S. aureus*. 250 $\mu\text{g}/\text{mL}$ of rGO/TiO_2 and 31.25 $\mu\text{g}/\text{mL}$ $\text{rGO}/\text{TiO}_2-\text{MnO}_x$ is suitable for *E. coli*, but 250 $\mu\text{g}/\text{mL}$ of TiO_2 is still not enough. All samples exhibit higher activity for the inhibition of *S. aureus* than *E. coli*. It is possible for *S. aureus* to be easily damaged during its merisis owing to the rougher cell membrane, as Shen et al. observed (seen TEM image in Ref. [63]). In addition, the bacterial colonies can be observed in L3 during the coating tests. The obvious comparison of bacterial colonies indicates some antibacterial effect of TiO_2 and MnO_x , and greater activity of rGO/TiO_2 and $\text{rGO}/\text{TiO}_2-\text{MnO}_x$. These results declare the synergism of graphene and MnO_x for promoting the activity of TiO_2 , in well accordance with the organic degradation in Fig. 7.

To evaluate accurately the bacteriostasis of GTM hybrids, the growth of *S. aureus* and *E. coli* with/no samples were further

studied, shown in Fig. 12. In control group, the typical lag phase can be observed in all-concentration tests within 4 h. The OD values of all-concentration suspensions show the inhibition against *S. aureus* and *E. coli* to varying degrees. The MIC of GTM hybrids for *S. aureus* and *E. coli* is found to be 15.62 $\mu\text{g}/\text{mL}$ and 62.5 $\mu\text{g}/\text{mL}$ (31.5–125 $\mu\text{g}/\text{mL}$ permitted), respectively. The higher MIC and $\text{OD}_{570\text{nm}}$ value of *E. coli* confirm the previous result that *S. aureus* is easier to inhibit. Two MIC evaluation methods suggest that GTM nanohybrids have a strong bacteriostasis effect at low MIC.

3.6. Mechanism analysis

To understand the mechanism of UV-preexcitation, Raman spectra and UV-vis diffused reflectance spectra of GTM hybrids in presence and absence of UV excitation were compared. After UV irradiation, the Raman spectra shows a clear change in the surface structure of GTM, as observed in Fig. 13a. In range of 100–1000 cm^{-1} , the peak intensity corresponding to TiO_2 decreased sharply owing to the formation of surface defects. In particular, a new broad peak is observed at around 700–900 cm^{-1} , which is attributed to the surface $\text{Ti}-\text{O}-\text{H}$ linkages in isolated $[\text{TiO}_4]$ or $[\text{TiO}_6]$ structural units [66,67]. The ratio of I_D/I_G in a-GTM ($I_D/I_G = 0.874$) is lower than the previous result ($I_D/I_G = 0.884$), confirming the further reduction of GO by UV irradiation. What is more, it can be seen from Fig. 13b that GTM nanohybrids displays broad absorption and several convex peaks (marked by circles) in both UV and visible light region. Based on the Kubelka–Munk formula, the bandgap (E_g) of rGO/TiO_2 , GTM, and a-GTM are 2.79, 2.62 and 2.25 eV, respectively. It means that graphene and MnO_x dots can narrow the bandgap of TiO_2 with a slow light effect for broad visible light absorption [53]. To our surprise, wider absorptions can be

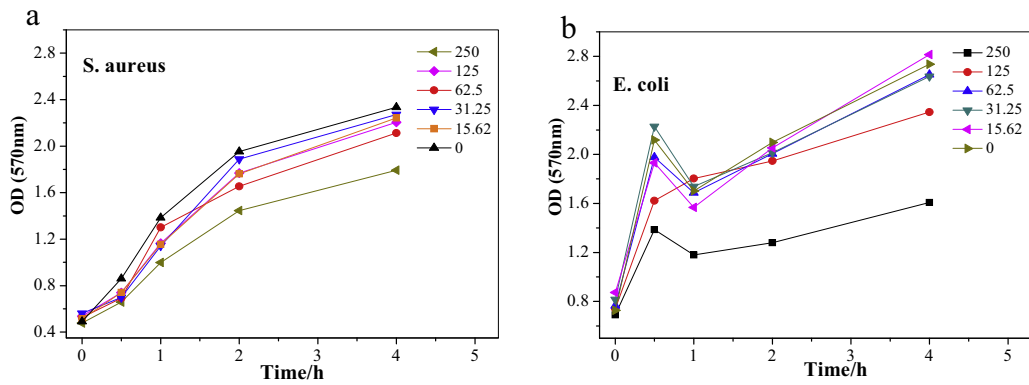


Fig. 12. (a) Growth curve study of bacterial strain *S. aureus* and (b) *E. coli* with different concentration of rGO/TiO₂–MnO_x hybrids.

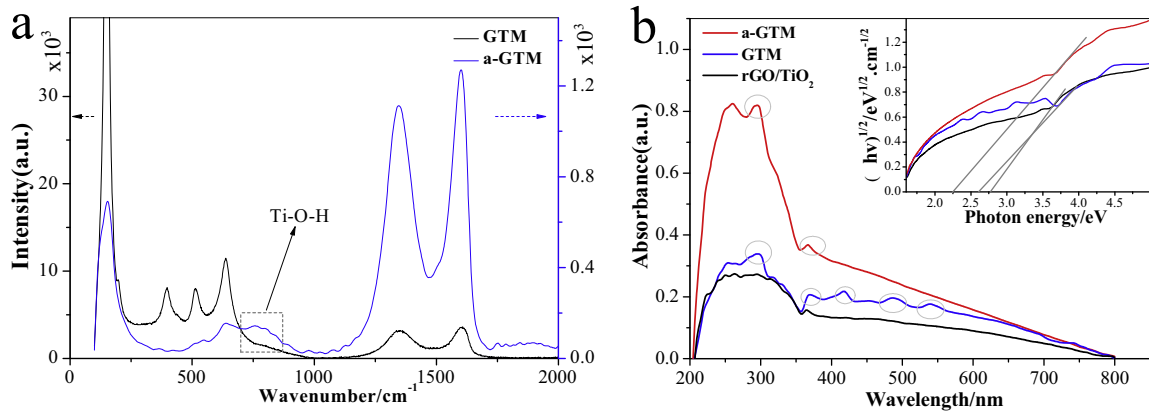


Fig. 13. (a) Raman of GTM in presence and absence of UV-preexcitation, (b) UV-vis diffused reflectance spectra and Kubelka–Munk transformation of GTM before and after UV-preexcitation.

observed in the diffused reflectance spectra of a-GTM, especially in the UV region. These results indicate that UV excitation can activate more surface and interface defects, such as O vacancy, Ti–O–C and Ti–O–H, extending the range of spectral response.

It is generally believed that the photocatalytic activity of semiconductors depends on the separation rate and ratio of photogenerated electron–hole pairs, which is negatively correlated with the PL intensity. Fig. 14 shows the PL spectra of different samples under the UV excitation wavelength at 260 nm. Main emission peaks of TiO₂ are aroused at 398 nm (3.12 eV) and 468 nm (2.6 eV), and importing graphene decreases the extinction

fluorescence intensity of TiO₂. Thus, graphene is conducive to improve the separation of electrons and holes. At the same time, the GTM without assistance of H₂O₂ shows some peak intensity decreases compared to that of TiO₂, and H₂O₂-treated GTM (L-GTM) has lower fluorescence extinction intensity. The comparison demonstrates that the generated O vacancies and Ti–OH by UV/H₂O₂ oxidation benefits to reduce the recombination of carriers since the O vacancies can elongate the electron conduction life and hinder the recombination [60]. The lowest PL intensity can be found in H-GTM hybrids. It should be originated from the electronic storage capacity of MnO_x, promoting the separation of charge carriers and quantum efficiency. These results confirm comparative photocatalytic activity of rGO/TiO₂ and L-GTM, but higher performance exists in H-GTM.

From the above results, it is clear that UV excitation can induce more surface defects (O vacancy and Ti–O–H) and reduce GO, thus enhancing the adsorbability, photocatalytic activity and durability of samples. The excellent property can correlate to the synergistic effect of high photocatalytic activity of TiO₂ and energy storage of MnO_x quantum dots as well as graphene conductive bridge. To better understand the photocatalytic mechanism of GTM and a-GTM hybrids, the schematic for the photocatalytic enhancement of rGO/TiO₂–MnO_x model was proposed and illustrated in Scheme 2. UV irradiation induces the O vacancy and Ti–OH on the surface, which broaden the light absorption, improve the adsorption of organics, and elongate the electron conduction life to separate the electron and hole pairs. Then photogenerated electrons can transfer rapidly from these surface capture points to graphene due to its excellent conductivity and possible to be further stored in crys-

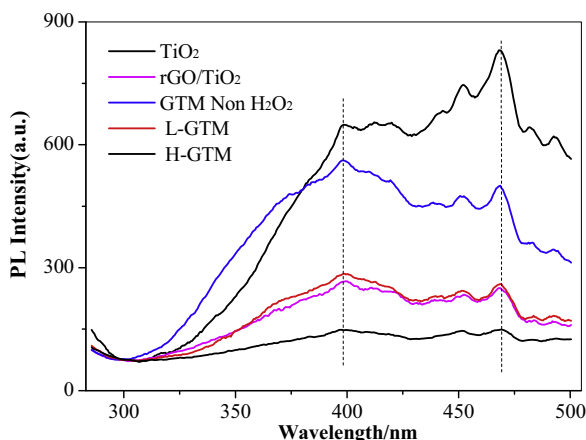
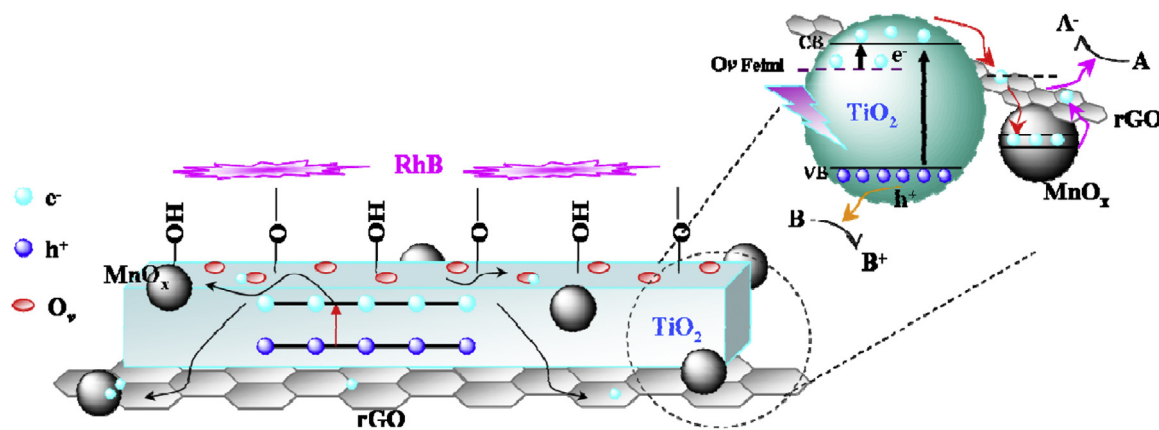


Fig. 14. Fluorescence emission spectra at 260 nm of different samples.



Scheme 2. Photocatalytic mechanism of GTM photochemical nanobattery model.

talline MnO_x dots. In addition, the surface amorphous MnO_x can capture and move the photoinduced holes of TiO_2 [68], hindering the recombination of charge carriers. When UV excitation stopped, the saved electrons can conduct along the graphene to join in catalysis [56,68]. Consequently, these following oxidative species (h^+ , O_2^- , $\cdot\text{OH}$ and HOOH) are prolonged and maintained in long time to mineralize organic dyes and microbial cells [69,70].

4. Conclusions

Decorating MnO_x QDs on reduced graphene oxide/ TiO_2 catalysts by combining UV excitation and microwave method is promising to obtain the higher photocatalytic and antibacterial activity. The as-prepared rGO/ TiO_2 - MnO_x nanobattery model possesses a low charge transfer resistance to separate the electron–hole pairs rapidly and some rewarding surface defects for a broad light absorption in the UV–vis region. The low Mn content, graphene usage about 6–10.0 mL and pH ~2.83 in the presence of H_2O_2 , is beneficial to deposit MnO_x QDs and obtain the optimal performance. Interestingly, the UV preexcitation is accessible to stronger adsorbability, photocatalytic durability and antibacterial activity by further activating the surface states and reducing graphene oxide. These findings suggest that UV excitation method has good potential in synthesis of materials and GTM hybrids support a supplement for rGO/ TiO_2 based photocatalysts using in wastewater treatment, solar cells and antibacterial agents. Despite many important discoveries, the controllable morphology and uniform loading of MnO_x quantum dots as well as the compatibility of electrochemistry and photocatalysis can be possible future directions, especially for the energy excitation methods.

Acknowledgements

This work is supported by Hunan Provincial Innovation Foundation For Postgraduate (No. CX2014B389) and Hunan Provincial Natural Science Foundation of China (No. 14JJ2077). Thanks the Open Fund of State Engineering Laboratory of Highway Maintenance Technology (No. kfj140106) and Open Research Fund Program of Key Laboratory of Water & Sediment Science and Water Hazard Prevention (Changsha University of Science & Technology) (No. 2015SS05).

References

- [1] J. Schneider, M. Matsuoka, M. Takeuchi, J. Zhang, Y. Horiuchi, M. Anpo, D.W. Bahnemann, *Chem. Rev.* 114 (2014) 9919–9986.
- [2] A. Hagfeldt, G. Boschloo, L. Sun, L. Kloo, H. Pettersson, *Chem. Rev.* 110 (2010) 6595–6663.
- [3] Z. Wang, H. Wang, B. Liu, W. Qiu, J. Zhang, S. Ran, H. Huang, J. Xu, H. Han, D. Chen, G. Shen, *ACS Nano* 5 (2011) 8412–8419.
- [4] J. Bai, B. Zhou, *Chem. Rev.* 114 (2014) 10131–10176.
- [5] X. Yang, J. Qin, Y. Li, R. Zhang, H. Tang, *J. Hazard. Mater.* 261 (2013) 342–350.
- [6] Q. Xiang, J. Yu, M. Jaroniec, *Chem. Soc. Rev.* 41 (2012) 782–796.
- [7] C. Huang, C. Li, G. Shi, *Energy Environ. Sci.* 5 (2012) 8848.
- [8] S. Morales-Torres, L.M. Pastrana-Martinez, J.L. Figueiredo, J.L. Faria, A.M. Silva, *Environ. Sci. Pollut. Res. Int.* 19 (2012) 3676–3687.
- [9] L.-L. Tan, W.-J. Ong, S.-P. Chai, A.R. Mohamed, *Appl. Catal. B: Environ.* 166–167 (2015) 251–259.
- [10] Y. Tang, S. Luo, Y. Teng, C. Liu, X. Xu, X. Zhang, L. Chen, *J. Hazard. Mater.* 241–242 (2012) 323–330.
- [11] B. Neppolian, A. Bruno, C.L. Bianchi, M. Ashokkumar, *Ultrason. Sonochem.* 19 (2012) 9–15.
- [12] Y. Wang, J. Yu, W. Xiao, Q. Li, *J. Mater. Chem. A* 2 (2014) 3847.
- [13] D. Zhang, Y. Gao, X. Pu, W. Li, C. Su, P. Cai, H.J. Seo, *Sci. Adv. Mater.* 6 (2014) 1–8.
- [14] T.-D. Nguyen-Phan, V.H. Pham, J.S. Chung, M. Chhowalla, T. Asefa, W.-J. Kim, E.W. Shin, *Appl. Catal. A: Gen.* 473 (2014) 21–30.
- [15] H. Li, Z. Xia, J. Chen, L. Lei, J. Xing, *Appl. Catal. B: Environ.* 168–169 (2015) 105–113.
- [16] J. Wang, P. Wang, Y. Cao, J. Chen, W. Li, Y. Shao, Y. Zheng, D. Li, *Appl. Catal. B: Environ.* 136–137 (2013) 94–102.
- [17] X. Yang, J. Qin, Y. Jiang, R. Li, Y. Li, H. Tang, *RSC Adv.* 4 (2014) 18627.
- [18] X. Yang, J. Qin, Y. Jiang, K. Chen, X. Yan, D. Zhang, R. Li, H. Tang, *Appl. Catal. B: Environ.* 166–167 (2015) 231–240.
- [19] Q. Xiang, J. Yu, M. Jaroniec, *J. Am. Chem. Soc.* 134 (2012) 6575–6578.
- [20] W. Han, C. Zang, Z. Huang, H. Zhang, L. Ren, X. Qi, J. Zhong, *Int. J. Hydrogen Energy* 39 (2014) 19502–19512.
- [21] G.S. Pozan, M. Isleyen, S. Gokcen, *Appl. Catal. B: Environ.* 140–141 (2013) 537–545.
- [22] Y. Huang, Y. Li, Z. Hu, G. Wei, J. Guo, J. Liu, *J. Mater. Chem. A* 1 (2013) 9809.
- [23] S. Chen, F. Liu, Q. Xiang, X. Feng, G. Qiu, *Electrochim. Acta* 106 (2013) 360–371.
- [24] K.A.M. Ahmed, H. Peng, K. Wu, K. Huang, *Chem. Eng. J.* 172 (2011) 531–539.
- [25] J. Qu, L. Shi, C. He, F. Gao, B. Li, Q. Zhou, H. Hu, G. Shao, X. Wang, J. Qiu, *Carbon* 66 (2014) 485–492.
- [26] C. He, B. Shen, J. Chen, J. Cai, *Environ. Sci. Technol.* 48 (2014) 7891–7898.
- [27] Y. Liu, T. Gu, X. Weng, Y. Wang, Z. Wu, H. Wang, *J. Phys. Chem. C* 116 (2012) 16582–16592.
- [28] T. Rhadfi, J.-Y. Piquemal, L. Sicard, F. Herbst, E. Briot, M. Benedetti, A. Atlamsani, *Appl. Catal. A: Gen.* 386 (2010) 132–139.
- [29] S. Li, Z. Ma, J. Zhang, Y. Wu, Y. Gong, *Catal. Today* 139 (2008) 109–112.
- [30] J. Guo, Q. Liu, C. Wang, M.R. Zachariah, *Adv. Funct. Mater.* 22 (2012) 803–811.
- [31] W. Wei, X. Cui, W. Chen, D.G. Ivey, *Chem. Soc. Rev.* 40 (2011) 1697–1721.
- [32] K. Dai, L. Lu, C. Liang, J. Dai, Q. Liu, Y. Zhang, G. Zhu, Z. Liu, *Electrochim. Acta* 116 (2014) 111–117.
- [33] Z. Lu, M. Meng, Y. Jiang, J. Xie, *Colloids Surf. A: Physicochem. Eng. Asp.* 447 (2014) 1–7.
- [34] Y.-L. Zhang, L. Guo, H. Xia, Q.-D. Chen, J. Feng, H.-B. Sun, *Adv. Opt. Mater.* 2 (2014) 10–28.
- [35] S. Cao, C. Chen, T. Liu, Y. Tsang, X. Zhang, W. Yu, W. Chen, *Chem. Eng. J.* 257 (2014) 309–316.
- [36] M. Baghbanzadeh, L. Carbone, P.D. Cozzoli, C.O. Kappe, *Angew. Chem.* 50 (2011) 11312–11359.
- [37] V.V. Kondalkar, S.S. Mali, N.B. Pawar, R.M. Mane, S. Choudhury, C.K. Hong, P.S. Patil, S.R. Patil, P.N. Bhosale, J.H. Kim, *Electrochim. Acta* 143 (2014) 89–97.
- [38] S.K. Meher, G.R. Rao, *J. Power Sources* 215 (2012) 317–328.
- [39] X. Pu, D. Zhang, Y. Gao, X. Shao, G. Ding, S. Li, S. Zhao, *J. Alloys Compd.* 551 (2013) 382–388.
- [40] A. Bello, O.O. Fashedemi, M. Fabiane, J.N. Lekitima, K.I. Ozoemena, N. Manyala, *Electrochim. Acta* 114 (2013) 48–53.
- [41] J.-S. Schanche, *Mol. Divers.* 7 (2003) 293–300.

[42] C. De Dobbelaere, J. Mullens, A. Hardy, M.K. Van Bael, *Thermochim. Acta* 520 (2011) 121–133.

[43] Q.-X. Liu, Z.-H. Zhou, *Polyhedron* 35 (2012) 1–6.

[44] W. Chen, L. Yan, P.R. Bangal, *Carbon* 48 (2010) 1146–1152.

[45] G. Jiang, Z. Lin, C. Chen, L. Zhu, Q. Chang, N. Wang, W. Wei, H. Tang, *Carbon* 49 (2011) 2693–2701.

[46] J. Sha, N. Zhao, E. Liu, C. Shi, C. He, J. Li, *Carbon* 68 (2014) 352–359.

[47] X. Lu, C. Song, S. Jia, Z. Tong, X. Tang, Y. Teng, *Chem. Eng. J.* 260 (2015) 776–784.

[48] C.M. Julien, M. Massot, C. Poinsignon, *Spectrochim. Acta Part A: Mol. Biomol. Spectrosc.* 60 (2004) 689–700.

[49] A. Ramadoss, S.J. Kim, *Int. J. Hydrogen Energy* 39 (2014) 12201–12212.

[50] Y. Wu, S. Liu, H. Wang, X. Wang, X. Zhang, G. Jin, *Electrochim. Acta* 90 (2013) 210–218.

[51] K.-H. Ye, Z.-Q. Liu, C.-W. Xu, N. Li, Y.-B. Chen, Y.-Z. Su, *Inorg. Chem. Commun.* 30 (2013) 1–4.

[52] J. Guo, S. Zhu, Z. Chen, Y. Li, Z. Yu, Q. Liu, J. Li, C. Feng, D. Zhang, *Ultrason. Sonochem.* 18 (2011) 1082–1090.

[53] D. Qi, L. Lu, Z. Xi, L. Wang, J. Zhang, *Appl. Catal. B: Environ.* 160–161 (2014) 621–628.

[54] G. Harichandran, S.D. Amalraj, P. Shanmugam, *J. Mol. Catal. A: Chem.* 392 (2014) 31–38.

[55] Y. Huang, J. Cai, Y. Guo, *Int. J. Hydrogen Energy* 37 (2012) 1263–1271.

[56] S. Obregón, G. Colón, *Appl. Catal. B: Environ.* 144 (2014) 775–782.

[57] J.Y. Liao, D. Higgins, G. Lui, V. Chabot, X. Xiao, Z. Chen, *Nano Lett.* 13 (2013) 5467–5473.

[58] Z. Zhang, F. Yu, L. Huang, J. Jiajiali, Y. Li, L. Song, N. Yu, D.D. Dionysiou, *J. Hazard. Mater.* 278 (2014) 152–157.

[59] H. Czili, A. Horváth, *Appl. Catal. B: Environ.* 81 (2008) 295–302.

[60] W. Fang, M. Xing, J. Zhang, *Appl. Catal. B: Environ.* 160–161 (2014) 240–246.

[61] S. Sontakke, J. Modak, G. Madras, *Appl. Catal. B: Environ.* 106 (2011) 453–459.

[62] H.U. Lee, S.C. Lee, S.M. Lee, J.W. Lee, H.J. Kim, J. Lee, *Appl. Catal. A: Gen.* 467 (2013) 394–399.

[63] S. Shen, T. Zhang, Y. Yuan, S. Lin, J. Xu, H. Ye, *Food Control* 47 (2015) 196–202.

[64] X. Lu, M. Yu, G. Wang, T. Zhai, S. Xie, Y. Ling, Y. Tong, Y. Li, *Adv. Mater.* 25 (2013) 267–272.

[65] Y. Luo, D. Kong, J. Luo, S. Chen, D. Zhang, K. Qiu, X. Qi, H. Zhang, C.M. Li, T. Yu, *RSC Adv.* 3 (2013) 14413.

[66] J. Su, G. Xiong, J. Zhou, W. Liu, D. Zhou, G. Wang, X. Wang, H. Guo, *J. Catal.* 288 (2012) 1–7.

[67] W. Song, Y. Zuo, G. Xiong, X. Zhang, F. Jin, L. Liu, X. Wang, *Chem. Eng. J.* 253 (2014) 464–471.

[68] R. Li, F. Zhang, D. Wang, J. Yang, M. Li, J. Zhu, X. Zhou, H. Han, C. Li, *Nature Commun.* 4 (2013) 1432.

[69] J.Y. Wu, C.W. Li, C.H. Tsai, C.W. Chou, D.R. Chen, G.J. Wang, *Nanomed.: Nanotechnol. Biol. Med.* 10 (2014) 1097–1107.

[70] R. Ahmad, M. Mohsin, T. Ahmad, M. Sardar, *J. Hazard. Mater.* 283 (2015) 171–177.